High-velocity impact damage behavior of plain-woven SiC/SiC composites after thermal loading

Yashiro, Shigeki
Department of Mechanical Engineering, Shizuoka University

Ogi, Keiji
Graduate School of Science and Engineering, Ehime University

Oshita, Masashi
Graduate School of Science and Engineering, Ehime University

出版情報：Composites Part B: Engineering. 43 (3), pp.1353-1362, 2012-04-01. Elsevier
バージョン：
権利関係：

High-velocity impact damage behavior of plain-woven SiC/SiC composites after thermal loading

S. Yashiro, K. Ogi, M. Oshita

PII: S1359-8368(11)00490-2
DOI: 10.1016/j.compositesb.2011.11.021
Reference: JCOMB 1569

To appear in: *Composites: Part B*

Received Date: 17 May 2011
Revised Date: 16 September 2011
Accepted Date: 1 November 2011

Please cite this article as: Yashiro, S., Ogi, K., Oshita, M., High-velocity impact damage behavior of plain-woven SiC/SiC composites after thermal loading, *Composites: Part B* (2011), doi: 10.1016/j.compositesb.2011.11.021

High-velocity impact damage behavior of plain-woven SiC/SiC composites after thermal loading

S. Yashiro [a,*], K. Ogi [b], and M. Oshita [b]

[a] Department of Mechanical Engineering, Shizuoka University

3-5-1 Johoku, Naka-ku, Hamamatsu 432-8561, Japan

[b] Graduate School of Science and Engineering, Ehime University

3 Bunkyocho, Matsuyama, Ehime 790-8577, Japan

* Corresponding author: Tel: +81-53-478-1026; Fax: +81-53-478-1026.

E-mail address: tsyashi@ipc.shizuoka.ac.jp (S. Yashiro)

Abstract

This study investigates characteristics of foreign-object damage in plain-woven SiC/SiC composites after thermal loading. High-speed impact tests were conducted on virgin specimens, thermally exposed specimens, and thermally shocked specimens, in which the maximum temperature during thermal loading was 600°C or 1000°C. An oxide layer was generated on the specimen surface by thermal loading at 1000°C. Damaged areas on the front and back surfaces induced by particle impact were independent of thermal loading. However, in specimens thermally loaded at 1000°C, brittle failure, i.e. cone cracking without fiber pull-out, occurred due to oxidation of the fiber/matrix interfaces, and the ballistic limit velocity significantly decreased. Finally, the ballistic limit is predicted using static strength properties, and the effect of thermal loading on impact resistance is discussed.

Keywords: A. Ceramic-matrix composites (CMCs); B. Impact behaviour; B. Environmental degradation; B. Embrittlement; Ballistic limit

1. Introduction

Ceramics have various advantages such as good thermal resistance, high modulus and strength, and a low thermal-expansion coefficient. However, they are brittle because of their high sensitivity to internal defects or damage. Ceramic matrix composites (CMCs) have been

developed by reinforcing ceramics with particles, whiskers, and fibers to improve damage tolerance. The bridging mechanism, i.e. fibers bridging matrix cracks, is the most important factor for high fracture toughness in CMCs. The fiber/matrix interface is debonded to prevent fiber breakage when matrix cracks reach fibers or fiber bundles. An appropriate cohesive strength of the fiber/matrix interface is required to achieve a phenomenon of fiber pullouts.

Woven CMCs in some cases exhibit higher fracture resistance than unidirectional or laminated CMCs and are expected to have extensive applications. Applying woven CMCs to high-temperature components of gas turbines will enable higher turbine inlet temperatures and improve efficiency [1-3]. However, high-speed impact of particles (foreign objects) is a key issue in practical use, since foreign-object damage (FOD) induces failure in high-temperature components such as rotating or stationary airfoils [4]. Therefore, high-speed impact tests have been conducted for some types of CMCs, and the damage characteristics, stiffness, and strength after impact have been investigated [5-9].

In order to use CMCs in high-temperature components, their FOD behavior at high temperatures should be clarified. Choi and co-workers [7,8] conducted high-speed impact tests of satin-woven SiC/SiC composites at room temperature and 1316°C using a burner rig, and reported that significant post-impact strength degradation but with little difference in damage size was observed. The authors [10] investigated the FOD behavior of three-dimensionally woven SiC/SiC composites at room temperature and 800°C, and observed embrittled damage characteristics in thermally exposed specimens. This embrittlement was ascribed to formation of the nanometer-scale oxidation layer at the fiber/matrix interface. However, studies on the FOD behavior of thermally loaded CMCs are limited, and the influence of thermal loading on FOD behavior has not been clarified.

This study investigates the FOD characteristics of thermally loaded plain-woven SiC/SiC composites. First, CMC specimens were thermally loaded under the following two conditions: (1) specimens were heated up to a given temperature and were gradually cooled; (2) specimens were heated up to a given temperature and were rapidly quenched. High-speed impact tests were conducted for as-received specimens (virgin specimens) and for thermally loaded specimens ((1) thermally exposed specimens; (2) thermally shocked specimens), and

damage patterns were observed. Finally, the ballistic limit velocity is predicted for thermally loaded CMCs, and the effect of thermal loading on impact resistance is discussed.

2. Experimental

2.1 Materials

The material used was plain-woven composites consisting of Si-Ti-C-O Tyranno™ fibers (Lox M) and a SiC-based matrix. Fiber interfaces were coated with a 10 nm SiO_x-rich layer surrounding an inner 40 nm carbon-rich layer [11]. Table 1 lists the material properties of Tyranno™ fibers. Each fiber bundle consists of 800 filaments, and the plain-woven fabrics were laminated as depicted in Fig. 1. Using polytitanocarbosilane as a precursor, a matrix was impregnated in the preform through eight cycles of polymer impregnation pyrolysis (PIP). The material was burned at 800°C and was heat-treated at 1200°C in a PIP cycle.

Two plates (Material #1 and Material #2) were used in this study. The fiber volume fraction was 38%, and there were eight layers for Material #1 and 10 layers for Material #2. Their thicknesses, densities, and void contents are listed in Table 2. The densities and void contents were measured by the Archimedian method.

2.2 Thermal-loading test

Thermal-exposure tests and thermal-shock tests were conducted on Material #1. The specimen size was 55 mm square (2.5 mm thick), which was the same as that for the impact tests. A thermocouple (type R) was attached to the specimen surface using heat-resistant ceramic adhesive to measure the specimen temperature. Specimens were heated by an infrared image furnace.

Figure 2 plots the temperature history of the specimen surface during thermal-loading tests. All specimens were heated up to a given temperature (600°C or 1000°C) at a constant heating rate of 50 K/min and were held at the given temperature for 30 minutes. After experiencing the maximum temperature, the specimens were gradually cooled in the furnace in the thermal-exposure tests. In the thermal-shock tests, specimens were quenched in to an oil bath of silicon oil (50°C). The distance from the specimen to the oil surface was less than 100 mm,

and the specimen was dropped vertically. Before and after the thermal-loading tests, the specimen surfaces and edges were observed by an optical microscope and a scanning electron microscope (SEM). There were five specimens for thermal exposure at 1000°C, five for thermal exposure at 600°C, five for thermal shock at 1000°C, and one for thermal shock at 600°C.

2.3 High-speed impact tests

High-speed impact tests were conducted on virgin specimens (Material #1 and Material #2), thermally exposed specimens (Material #2), and thermally shocked specimens (Material #2).

Figure 3 is a schematic diagram of a high-speed impact testing machine (Maruwa Electronic Incorporated). A projectile set in a sabot was accelerated with high-temperature, high-pressure metal plasma obtained by melting and evaporating aluminum foil (2 mm × 60 mm) subjected to high-voltage (3 to10 kV) pulse current. The sabot was stopped at the mouth of the gun, and inertia carried the projectile forward. The projectile velocity was controlled by the voltage applied to the aluminum foil.

A steel ball of the type used for bearings with a diameter of 2.5 mm (0.0623 g) was used as the projectile. The four edges of each of 55-mm square target specimens were rigidly clamped by a fixture jig as shown in Fig. 4a. A 50 mm square hollow existed at the back of the fixed specimen (Fig. 4b), and bending deformation due to impact loading was permitted.

Acceleration sensors were mounted on the mouth of the gun and the fixture jig, and the time interval after projection from the sabot before impact was measured to calculate the projectile velocity. The range of the impact velocity v was 100 to 600 m/s. There were seven virgin specimens of Material #1. For thermally loaded specimens of Material #2, there were five virgin specimens, five for thermal exposure at 1000°C, six for thermal exposure at 600°C, five for thermal shock at 1000°C, and five for thermal shock at 600°C.

2.4 Damage observation

After the impact tests, damage patterns on the impact surface and the back surface were

observed by a stereomicroscope, and the damage area was measured using image-processing software. The specimens were then cut and polished, and damage beneath the impact point was observed using an optical microscope. Moreover, internal damage was nondestructively imaged using a micro-focus X-ray CT system (TOSCANER-3000μhd, Toshiba IT & Control Systems Corporation) for some specimens.

3. Experiment results and discussion

3.1 Damage after thermal loading

Figure 5 presents SEM images of the specimen edges before and after thermal loading at 1000°C. The edge tarnished after thermal loading, even if the surface was polished to a mirror surface. This observation suggested the generation of an oxide layer, to be described later. Fibers were chipped off in both the thermally exposed and thermally shocked specimens. Furthermore, pores were generated between fibers in the thermally shocked specimen.

3.2 High-speed impact damage

3.2.1 Virgin specimens

Figure 6 depicts typical damage patterns on the front (impact) surface and the back surface of virgin specimens. A crater was generated and a slight bump and fiber breaks were observed around the crater at impact velocity v = 100 m/s (Fig. 6a); no damage occurred on the back surface. At v = 150 m/s (Fig. 6b), a bump and fiber breaks as well as a crater were generated on the front surface, similar to those in Fig. 6a, and bumps were observed beneath the impact point on the back surface. At v = 350 m/s (Fig. 6c), a penetration hole with bumps and fiber breaks was generated on the front surface, and bumps and fiber breaks were observed over a large area near the penetration hole on the back surface.

Figure 7 depicts internal damage in the above-observed specimens inspected using an X-ray CT system. In all of the specimens, a cone crack extended from the crater edge. Severe damage with interfacial debonding, matrix cracks, and fiber breaks was observed inside the cone crack region at v = 150 m/s (Fig. 7b). Fiber/matrix interfacial debonding was observed near the cone crack at v = 350 m/s (Fig. 7c). The projectile bounced back from the specimen

at v = 350 m/s, and the damage in Fig. 7c was in fact spall damage in which the cone crack penetrated the thickness of the specimen.

Figure 8 plots the relationship in projected damage area between the front and the back surfaces as a function of impact velocity. Here, the damaged region was divided into the crater and the damage in the neighboring area (peripheral damage); the area of the penetration hole was counted as part of the crater. The sum of the areas of the crater and the peripheral damage is also plotted as all damage. The vertical line in Fig. 8 represents the penetration limit velocity of the damage at which damage appeared on the back surface, and the horizontal line represents the projected area of the projectile. The peripheral damage area, as well as the total damage area, increased on the front surface with increasing impact velocity regardless of penetration. The crater area increased up to the penetration limit and converged to the projected area of the projectile (≈ 5 mm^2) over the limit velocity. The damaged area on the back surface was larger than that of the front surface. The area of the penetration hole (the crater in Fig. 8b) on the back surface was almost a constant value (8 mm^2), since the angle of the cone crack changed only slightly in the velocity range of this study. The peripheral damage area was approximately constant (17 mm^2).

3.2.2 Thermally loaded specimens

Figure 9 illustrates the classification of the pattern of damage at several impact velocities for the thermally exposed and thermally shocked specimens. The maximum temperature during thermal loading is presented on the vertical axis, and the data at room temperature represents the results for virgin specimens. Although the impact response of woven CMCs could have stochastic aspects, the impact damage was classified into four patterns: (1) damage was generated on the front surface only; (2) damage reached the back surface; (3) perforation occurred but the projectile bounced back; and (4) perforation occurred and the projectile penetrated the target. For specimens thermally loaded at 600°C, the ballistic limit, i.e. the velocity at which the projectile penetrated the specimen, was 250 to 350 m/s regardless of the thermal-loading type, and was similar in range to that for virgin specimens. However, for specimens thermally loaded at 1000°C, the projectile penetrated the specimen at a velocity

less than 150 m/s, and the impact resistance was significantly degraded. This result suggests that the primary factor affecting the impact resistance was not the state of thermal stresses during cooling but the maximum holding temperature during the thermal loading.

Figure 10 depicts the damage states on the front and back surfaces of all of the specimens impacted at velocities over the ballistic limit. Fibers were raised near the penetration hole on both front and back surfaces in the virgin specimen (Fig. 10a) and the specimen thermally exposed at 600°C (Fig. 10b). The outermost layer peeled off of the back surface and fibers of the inner layers were observed in the specimen thermally shocked at 600°C (Fig. 10c), although fibers were raised similarly to Fig. 10b. A sharp-edged penetration hole without projection of fibers was generated in specimens thermally loaded at 1000°C (Figs. 10d, 10e).

Figure 11 presents cross-section images beneath the impact point observed by an optical microscope, in which the specimens are the same as in Fig. 10. The bridging mechanism functioned, and fiber pull-out occurred on the surface of the cone crack in the virgin specimen (Fig. 11a) and in the specimens thermally loaded at 600°C (Figs. 11b, 11c), which resulted in the projection of fibers observed in Figs. 10a-10c. However, in the specimens thermally loaded at 1000°C (Figs. 11d, 11e), the cone crack extended in a straight line without fiber pull-out. This damage state was a typical failure pattern of brittle CMCs. Moreover, a few outermost layers peeled off in the specimens thermally loaded at 1000°C, although the spall broke into small pieces in the other specimens. This difference suggests embrittlement in the specimens thermally loaded at 1000°C.

Figure 12 plots the projected damage area on the front and back surfaces of all of the specimens. The damage area on the front surface increased in proportion to the impact velocity regardless of thermal loading type. Moreover, no significant difference in the damage area on the back surface was observed among all of the specimen types, although the data varied widely.

3.3 Discussion

The brittle FOD characteristics in thermally loaded specimens suggest a change in the strength of the fiber/matrix interface due to thermal loading. Since the carbon layer

surrounding the fibers was oxidized by exposing the specimens to air at 1000°C, the interface was strongly adhered between fibers and matrix, resulting in strong interface rather than weak interface [10,12]. In this case, primary cracks generated in the matrix hardly induced debonding when they reached the fiber/matrix interfaces, and fibers broke concurrently with crack extension. The embrittlement after thermal loading was clearly reflected in static strength. Figure 13 depicts load-displacement curves in four-point flexural loading-unloading tests for specimens with and without thermal loading at 1000°C. The specimens were 60 mm long, 10 mm wide, and 2.6 mm thick. The inner (outer) span was 20 mm (50 mm). Although quasi-ductile characteristics were observed in virgin specimens, thermally loaded specimens exhibited brittle fracture, and their bending strengths were much lower than that of virgin specimens. Therefore, thermal loading resulted in a degradation of the tensile strength of the SiC/SiC composites. Indeed, a straight cone crack without fiber pull-out, which is evidence of fiber/matrix fixture, was observed in the specimens thermally loaded at 1000°C (Fig. 11). These results indicate that the ballistic limit was degraded by embrittlement of the interface.

The ballistic limit velocity V_b can be predicted from the static strength properties, following a semi-empirical energy-based approach proposed by Wen [13]. Although this analysis was applied to FPRs and the FOD characteristics of CMCs differed from those of FRPs, its formulation was independent of the material system or impact mechanism. This analysis could therefore be used for any material system if an appropriate value of the empirical constant β (described later) is used. The pressure in the target imposed by the projectile, σ, is divided into a static term σ_s involving elastic-plastic deformation and a dynamic term σ_d that resulted from the impact velocity v. It was assumed that the static term was equal to the elastic limit σ_e, and that the dynamic term was a function of a parameter $(\rho_t/\sigma_e)^{1/2}v$, where ρ_t was the density of the target. Here, the total pressure σ is expressed as

$$\sigma = \left(1 + \beta\sqrt{\frac{\rho_t}{\sigma_e}}\,v\right)\sigma_e, \tag{1}$$

where β is an empirical constant concerning the shape of the projectile. Considering the work done by the total pressure σ, the initial kinetic energy of the projectile required to penetrate the target, E_k, is

$$E_k = \frac{\pi D^2 T \sigma_e}{4}\left(1+\beta\sqrt{\frac{\rho_t}{\sigma_e}}V_b\right), \tag{2}$$

where D is the diameter of the projectile and T is the thickness of the target. The first term on the right-hand side represents the static indentation at a pressure equal to the elastic limit; the second term represents the increase of the pressure due to dynamic phenomena as well as the energy absorption by damage extension to the peripheral region. Substituting the kinetic energy of the projectile $E_k = (1/2)mV_b^2$ into Eq. (2), where m is the mass of the projectile, the ballistic limit velocity V_b is obtained as follows.

$$V_b = \frac{\pi\beta\sqrt{\rho_t\sigma_e}D^2T}{4m}\left(1+\sqrt{1+\frac{8m}{\pi\beta^2\rho_t D^2 T}}\right) \tag{3}$$

The constant β is 1.5 for projectiles with hemispherical ends [13], and $\beta = 1.2$ is assumed for a spherical projectile, considering the volume ratio. The elastic limit is obtained from the load-displacement curve in four-point bending tests (Fig. 13) and was the maximum bending stress of the linear region. The elastic limit in the specimens thermally loaded at 1000°C was equal to the breaking stress, since no damage occurred until final failure.

Table 3 lists the predicted ballistic limit velocity of the virgin specimen and the specimens thermally loaded at 1000°C, along with the experiment results. The prediction agreed well with the experiment for the virgin specimen. However, the predictions for the thermally loaded specimens significantly differed from the experiment results. Figure 14a plots the ballistic limit velocity against the elastic limit. It was found that the reduction of the ballistic limit could not be represented solely by the change in the static strength property σ_e, and that the damage extension characteristics should be considered in Eq. (2). The energy absorption due to damage extension was small in the thermally loaded specimens, since fiber pull-out hardly occurred. Taking this observation into account, the second term on the right-hand side of Eq. (2) was multiplied by a coefficient C, which captures the effects of energy absorption due to damage extension to the peripheral region.

$$E_k = \frac{\pi D^2 T \sigma_e}{4}\left(1+C\beta\sqrt{\frac{\rho_t}{\sigma_e}}V_b\right) \tag{4}$$

If no internal damage was assumed (C=0), the ballistic limit velocity was

$$V_b = D\sqrt{\frac{\pi T \sigma_e}{2m}}\,. \tag{5}$$

Predictions made using Eq. (5) agreed with the experiments for thermally loaded specimens (Table 3, Fig. 14a). The input energy can be divided into that required for penetration, projectile deformation and/or fracture, target delamination or cracking, and rebounding of the projectile. Here, Eq. (5) considers only the work at pressure σ_e during target penetration, and the energy absorption by projectile deformation and the remaining kinetic energy of the projectile were disregarded. It was then found that the energy absorbed by the projectile was not dominant.

This approach to predicting the ballistic limit was applied to three-dimensionally orthogonally woven SiC/SiC composites (3D-CMC) consisting of the same fibers and matrix. Figure 14b illustrates the predicted ballistic limit velocity along with the experiment results for virgin and the thermally exposed (800°C) 3D-CMCs (T = 6 mm) [10]. Here, the elastic limits were obtained by bending tests, and were 172 MPa (virgin) and 171 MPa (thermally exposed at 800°C). Although these elastic limits were almost the same, the ballistic limit of the virgin specimen agreed with a prediction based on Eq. (3), and that of the thermally exposed specimen was intermediate between Eqs. (3) and (5). Here, fiber pull-out was observed in the fracture surface of the bent thermally exposed specimen, although the specimens were embrittled and the breaking strength was degraded [10]. This failure pattern suggests that the fiber/matrix interface was not entirely fixed. Therefore, it was deemed appropriate to consider damage extension in the target ($0<C<1$) when predicting the ballistic limit velocity. For thermally exposed specimens, the prediction coincided with the experiment when the energy absorption by damage extension slightly decreased (C=2/3). These results indicate that reduction of the ballistic limit in thermally loaded specimens is caused by a decrease in energy absorption due to internal damage extension, as well as by degradation of the static strength.

4. Conclusions

This study investigated the effects of thermal loading on FOD behavior in plain-woven

SiC/SiC composites. Specimens were thermally exposed or thermally shocked, with maximum temperatures during thermal loading of 600°C or 1000°C. High-speed impact tests were then conducted, and the resulting damage state was observed in detail. Our conclusions are summarized below.

1. An oxide layer was generated on the specimen surface by thermal loading at 1000°C. Fiber chipping and gaps between fibers were also generated.
2. The ballistic limit velocity of specimens thermally loaded at 600°C was almost the same as that of virgin specimens. However, the impact resistance of specimens thermally loaded at 1000°C was significantly degraded from that of the virgin specimens. Therefore, the maximum temperature during thermal loading was the primary factor affecting the impact resistance.
3. The projected damage area on the front (back) surface was independent of thermal loading, and varied with the impact velocity.
4. Fibers were pulled out near the penetration hole, and the fiber/matrix interface was debonded near the cone crack in the specimens thermally loaded at 600°C. The brittle fracture characteristics, i.e. no fiber pull-out and straight cone cracks, were observed in the specimens thermally loaded at 1000°C.
5. A comparison between the theoretical ballistic limit velocity and the experiment results indicates that the ballistic limit was degraded by thermal loading because of embrittled damage extension behavior and degraded static strength, both of which occurred due to the fixture of the fiber/matrix interface.

It should be noted that this embrittlement due to thermal loading would be avoidable by treatment with appropriate thermal/environmental barrier coating.

Acknowledgement

Part of this research was supported by Grants-in-Aid (Nos. 20760071, 21360417 and 22760524) for Scientific Research from the Ministry of Education, Science, Sports and Culture of Japan.

References

[1] Ohnabe H, Masaki S, Onozuka M, Miyahara K, Sasa T. Potential application of ceramic matrix composites to aero-engine components. Composites Part A 1999; 30(4):489-496.

[2] Kaya H. The application of ceramic-matrix composites to the automotive ceramic gas turbine. Compos Sci Technol 1999; 59(6):861-872.

[3] Naslain R. Design, preparation and properties of non-oxide CMCs for application in engines and nuclear reactors: an overview. Compos Sci Technol 2004; 64(2):155-170.

[4] Wiederhorn SM, Ferber MK. Silicon nitride for gas turbines. Curr Opin Solid State Mat Sci 2001; 5(4):311-316.

[5] Boccaccini AR, Atiq S, Boccaccini DN, Dlouhy I, Kaya C. Fracture behaviour of mullite fibre reinforced-mullite matrix composites under quasi-static and ballistic impact loading. Compos Sci Technol 2005; 65(2):325-333.

[6] Bhatt RT, Choi SR, Cosgriff LM, Fox DS, Lee KN. Impact resistance of environmental barrier coated SiC/SiC composites. Mater Sci Eng A 2008; 476(1-2):8-19.

[7] Bhatt RT, Choi SR, Cosgriff LM, Fox DS, Lee KN. Impact resistance of uncoated SiC/SiC composites. Mater Sci Eng A 2008; 476(1-2):20-28.

[8] Choi SR. Foreign object damage phenomenon by steel ball projectiles in a SiC/SiC ceramic matrix composites at ambient and elevated temperatures. J Am Ceram Soc 2008; 91(9):2963-2968.

[9] Choi SR, Alexander DJ, Kowalik RW. Foreign object damage in an oxide/oxide composite at ambient temperature. J Eng Gas Turb Power 2009;131:021301-1–0212301-6.

[10] Ogi K, OkabeT, Takahashi M, Yashiro S, Yoshimura A, Ogasawara T. Experimental characterization of high-speed impact damage behavior in a three-dimensional woven SiC/SiC composite. Composites Part A 2010; 41(4): 489-498.

[11] Ogasawara T, Ishikawa T, Matsuzaki T. Thermal response and oxidation of Tyranno^{TM}-fiber-reinforced Si-Ti-C-O matrix composites for a thermal protection system in high-enthalpy dissociated air. J Am Ceram Soc 2003; 86(5):830-837.

[12] Davies IJ, Ishikawa T, Shibuya M, Hirokawa T. Fibre strength parameters measured in situ for ceramic-matrix composites tested at elevated temperature in vacuum and in air.

Compos Sci Technol 1999; 59(6):801-811.

[13] Wen HM. Predicting the penetration and perforation of FRP laminates struck normally by projectiles with different nose shapes. Compos Struct 2000; 49(3):321-329.

Figure caption

Fig. 1 Surface and cross-sectional views of the plain woven SiC/SiC composite.

Fig. 2 Time history of the specimen temperature during thermal exposure tests and thermal shock tests.

Fig. 3 Schematic diagram of the high-speed impact testing machine.

Fig. 4 Fixture of the target specimen: (a) overview, and (b) schematic diagram.

Fig. 5 SEM images of the specimen edge before and after thermal loading.

Fig. 6 Surface-damage states of impacted virgin specimens.

Fig. 7 X-ray CT images of impacted virgin specimens. The specimens correspond to those in Fig. 6.

Fig. 8 Relation between projected damage area and impact velocity for virgin specimens.

Fig. 9 Temperature-impact velocity diagram for classification of impact damage. Penetration limit velocity, at which the projectile penetrated the target, was estimated from both of thermally exposed and thermally shocked specimens.

Fig. 10 Damage states on the front and back surfaces of specimens impacted at velocities exceeding the ballistic limit.

Fig. 11 Damage in the cross-section beneath the impact point for specimens impacted at velocities exceeding the ballistic limit.

Fig. 12 Relation between the projected damage area and impact velocity for all thermal-loading types.

Fig. 13 Typical load-displacement curves from four-point flexural loading-unloading tests.

Fig. 14 A comparison of the theoretical prediction of the ballistic limit with the experiment for virgin and thermally loaded specimens.

Table 1 Material properties in Tyranno-fiber (Lox-M).

Tensile strength (GPa)	3.3
Fracture elongation (%)	1.8
Density (g/cm^3)	2.48
Filament diameter (μm)	11
Filament number (number/bundle)	800
Thermal conductivity (W/m/K)	1.4

Table 2 Material properties of plain-woven SiC/SiC composites.

	Thickness (mm)	Density (g/cm^3)	Porosity (%)
Material #1	2.5	2.3	8.6
Material #2	3.5	2.1	15.7

Table 3 Prediction of the ballistic limit.

Specimen type	Elastic limit (MPa) σ_e *1	Ballistic limit (m/s) Prediction by Eq. (3)	Ballistic limit (m/s) Prediction by Eq. (5)	Ballistic limit (m/s) Experiment *2
Virgin	43.8	286	N/A	278
Thermal exposure at 1000°C	27.9	228	124	< 128
Thermal shock at 1000°C	27.8	227	124	154

*1 Obtained by four-point bending tests.

*2 Minimum impact velocity at which the projectile penetrated the target.

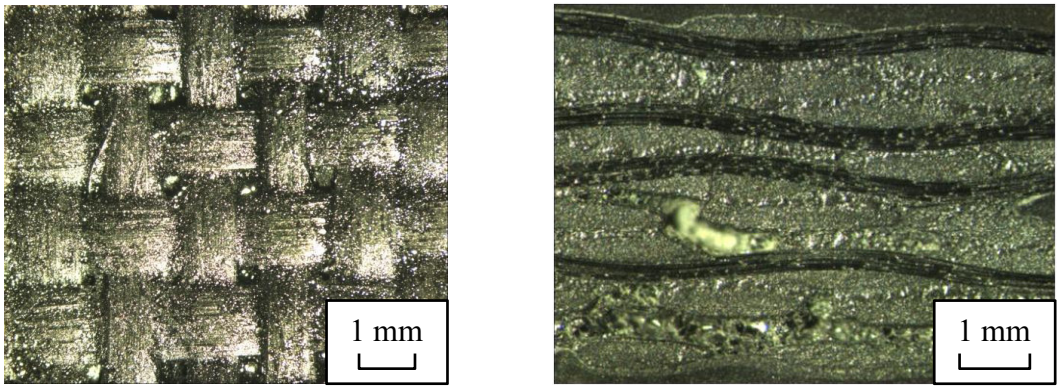

(a) Surface (b) Cross-section

Fig. 1 Surface and cross-sectional views of the plain woven SiC/SiC composite.

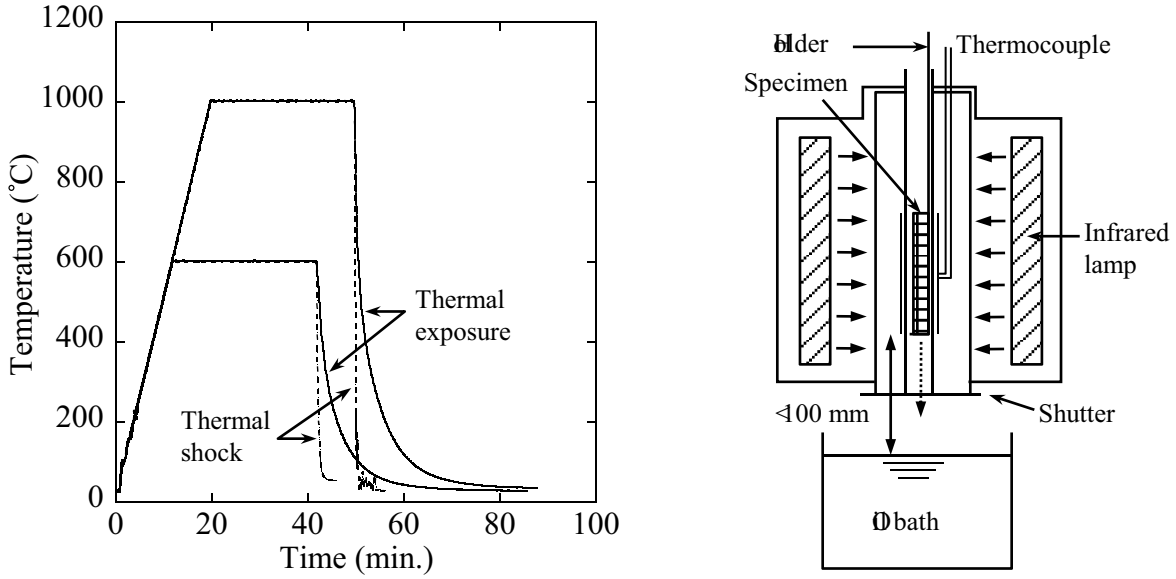

(a) Specimen temperature (b) Schematic of the thermal shock test

Fig. 2 Time history of the specimen temperature during thermal exposure tests and thermal shock tests.

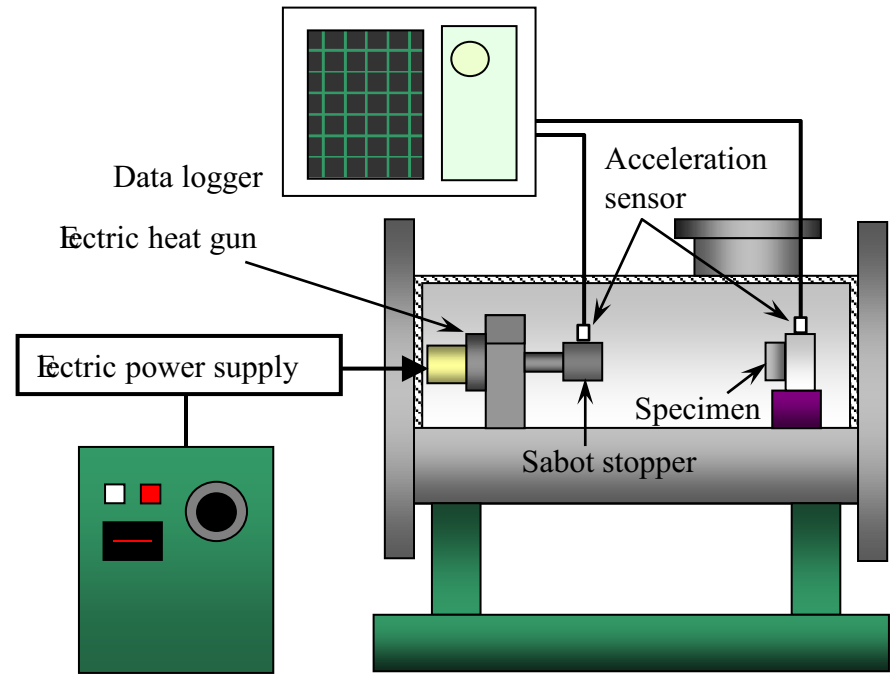

Power source control panel Chamber

Fig. 3 Schematic diagram of the high-speed impact testing machine.

(a)

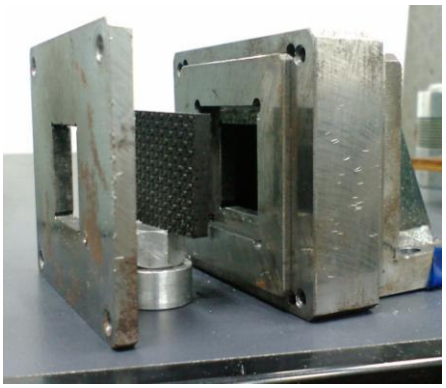

(b)

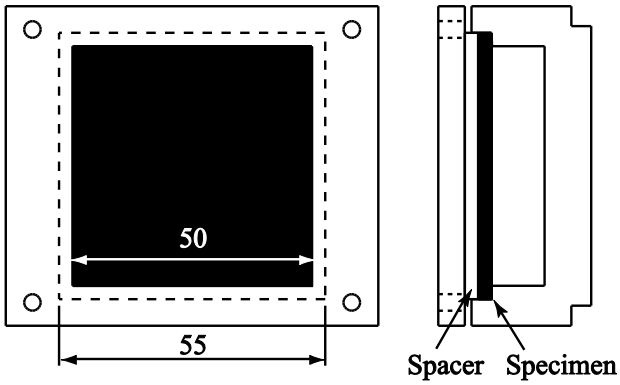

Fig. 4 Fixture of the target specimen: (a) overview, and (b) schematic diagram.

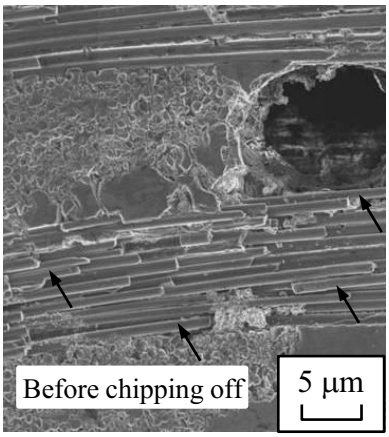

(a) Before thermal exposure

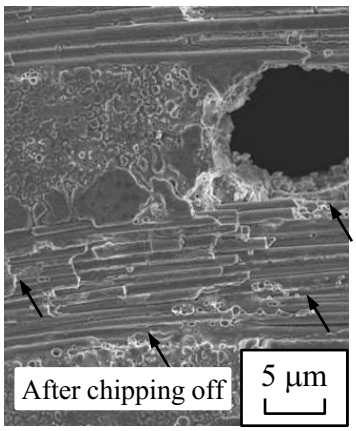

(b) After thermal exposure at 1000ºC

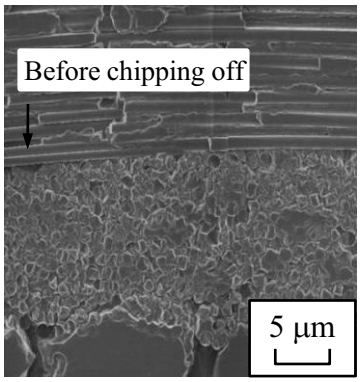

(c) Before thermal shock

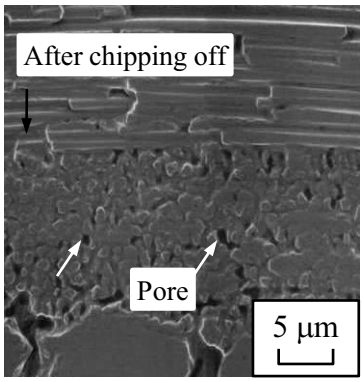

(d) After thermal shock at 1000ºC

Fig. 5 SEM images of the specimen edge before and after thermal loading.

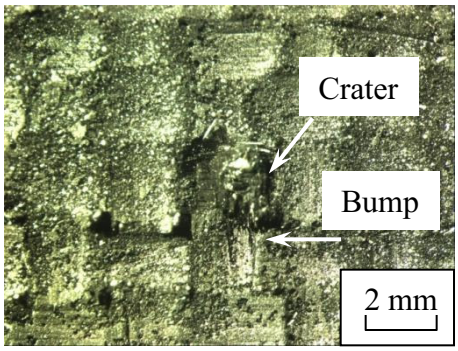

(a) v = 100 m/s (front)

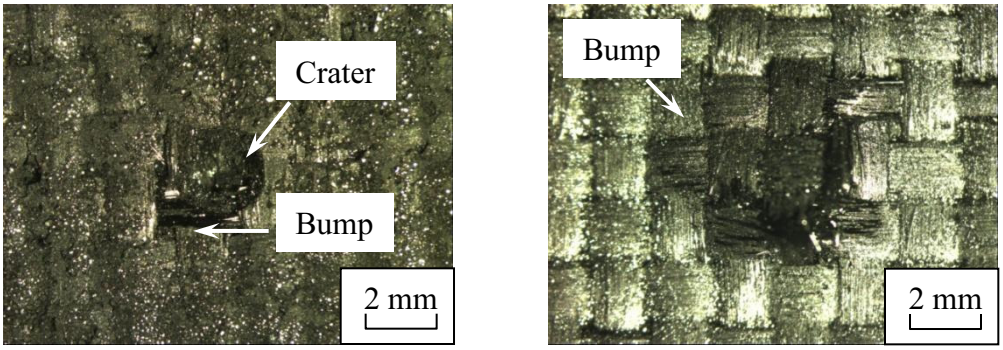

(b) v = 150 m/s (left: front, right: back)

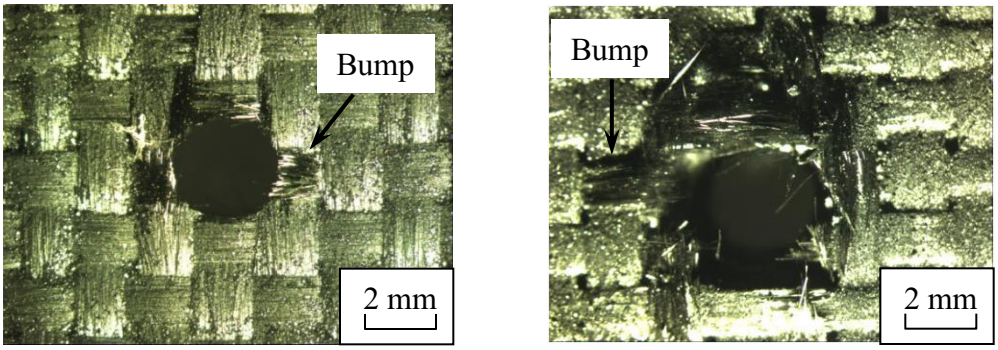

(c) v = 350 m/s (left: front, right: back)

Fig. 6 Surface-damage states of impacted virgin specimens.

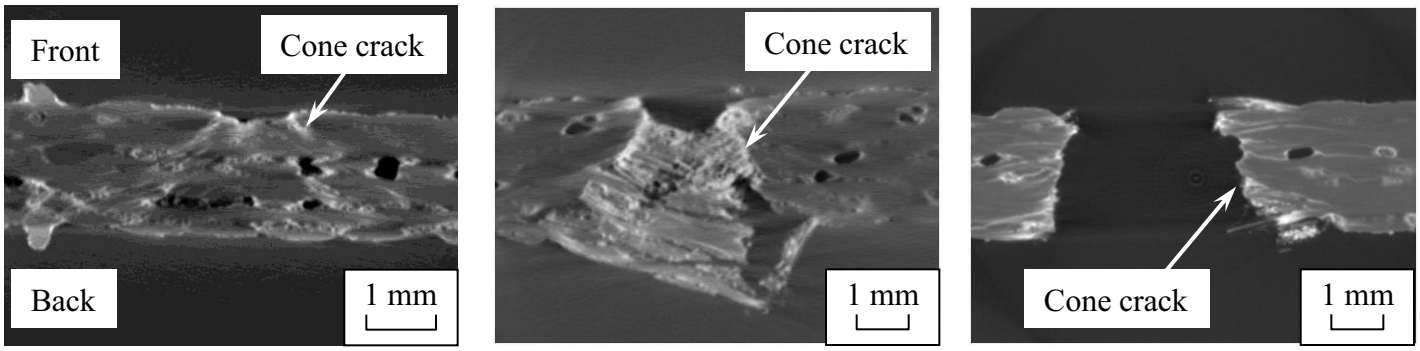

(a) v = 100 m/s (b) v = 150 m/s (c) v = 350 m/s

Fig. 7 X-ray CT images of impacted virgin specimens. The specimens correspond to those in Fig. 6.

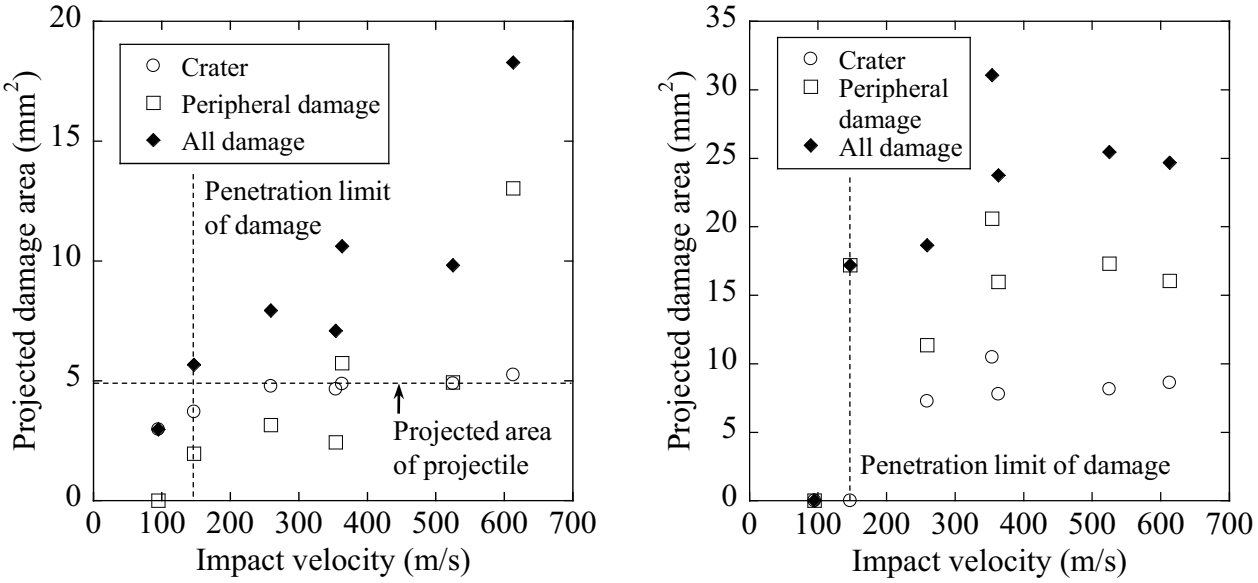

(a) Front surface (b) Back surface

Fig. 8 Relation between projected damage area and impact velocity for virgin specimens.

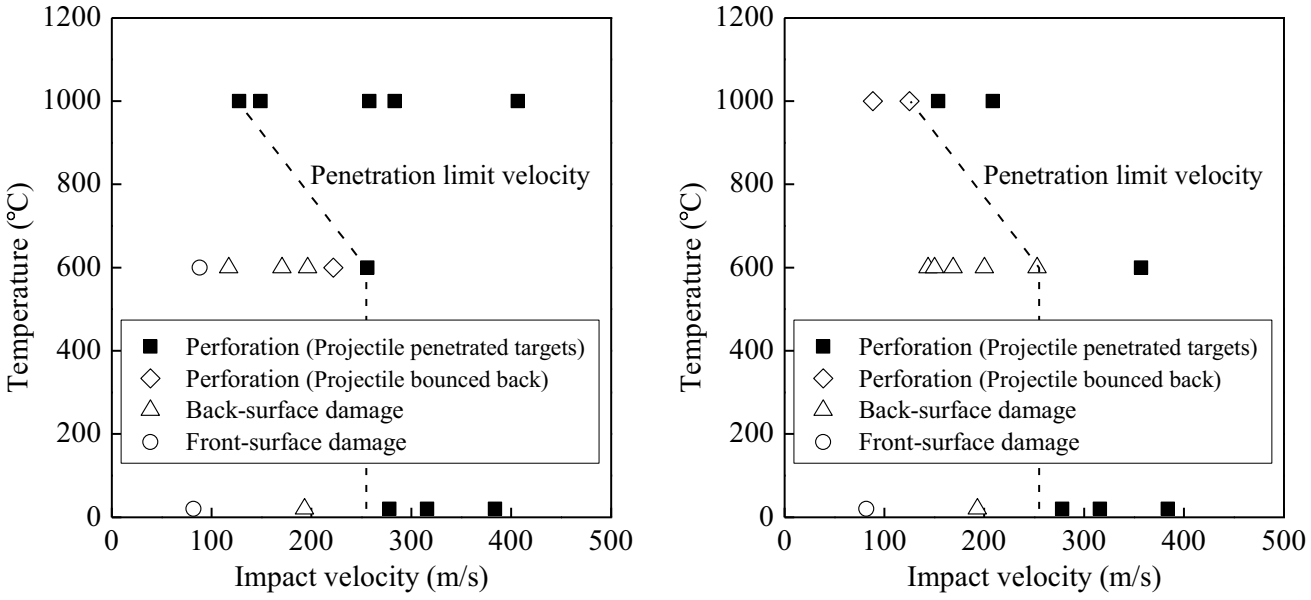

(a) Thermally exposed specimen (b) Thermally shocked specimen

Fig. 9 Temperature-impact velocity diagram for classification of impact damage. Penetration limit velocity, at which the projectile penetrated the target, was estimated from both of thermally exposed and thermally shocked specimens.

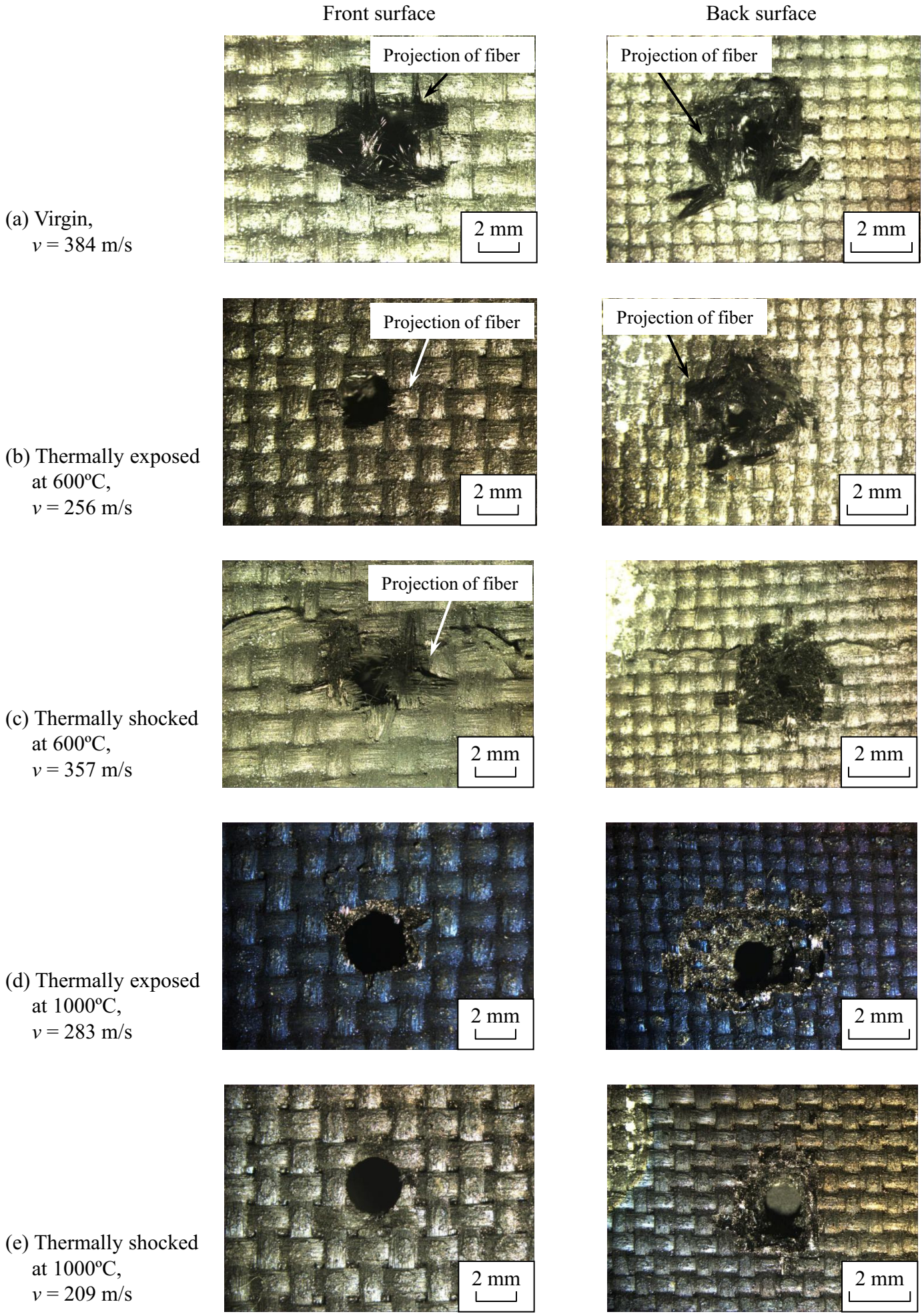

Fig. 10 Damage states on the front and back surfaces of specimens impacted at velocities exceeding the ballistic limit.

(a) Virgin,
v = 384 m/s

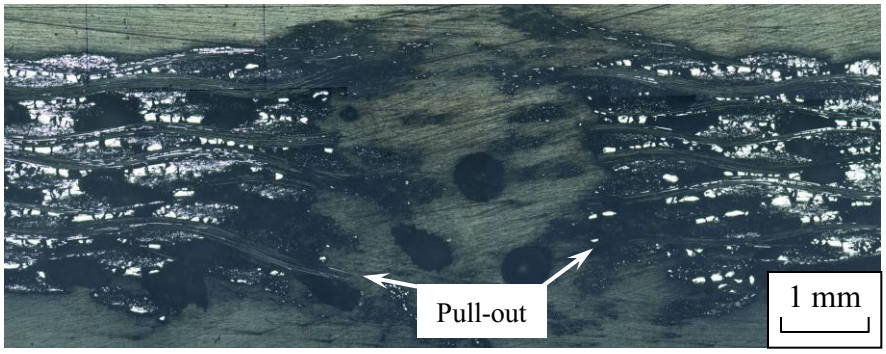

(b) Thermally exposed
at 600ºC,
v = 256 m/s

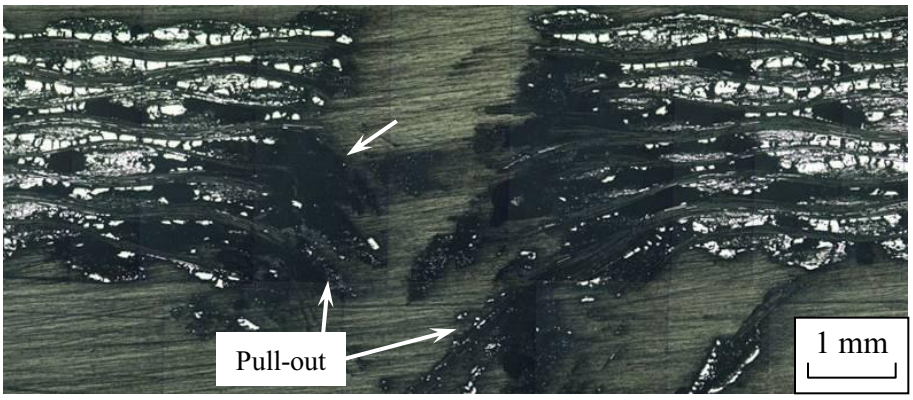

(c) Thermally shocked
at 600ºC,
v = 357 m/s

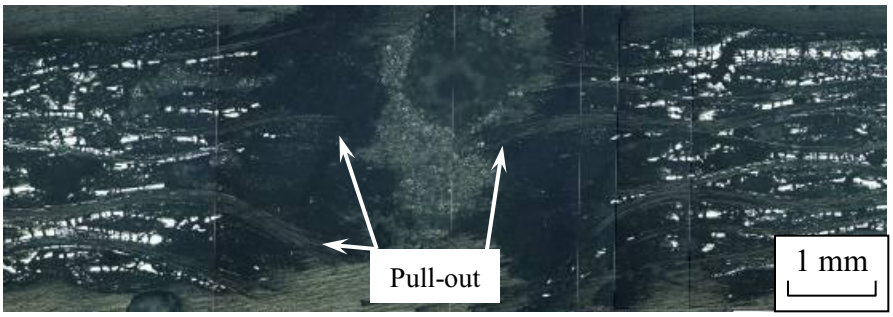

(d) Thermally exposed
at 1000ºC,
v = 283 m/s

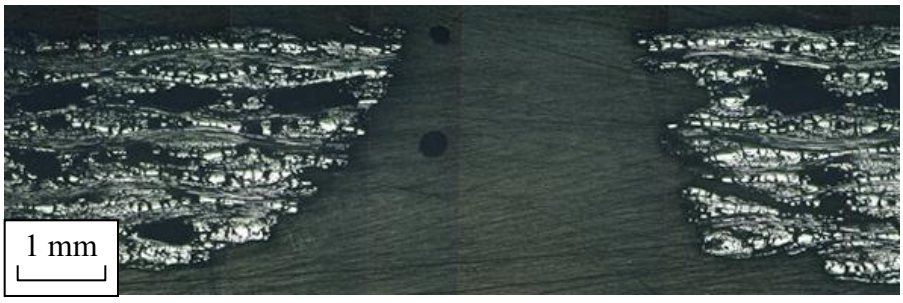

(e) Thermally shocked
at 1000ºC,
v = 209 m/s

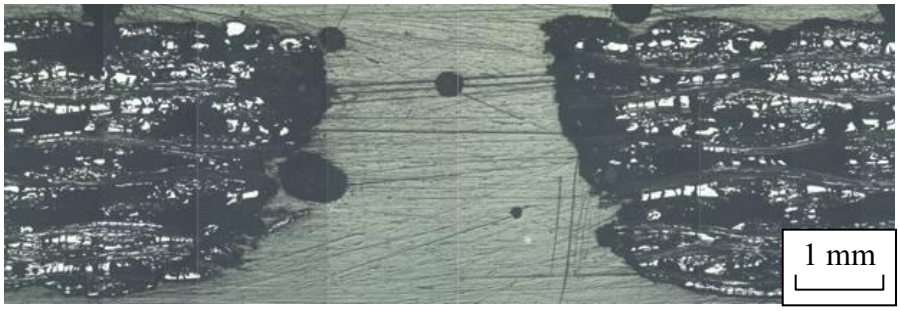

Fig. 11 Damage in the cross-section beneath the impact point for specimens impacted at velocities exceeding the ballistic limit.

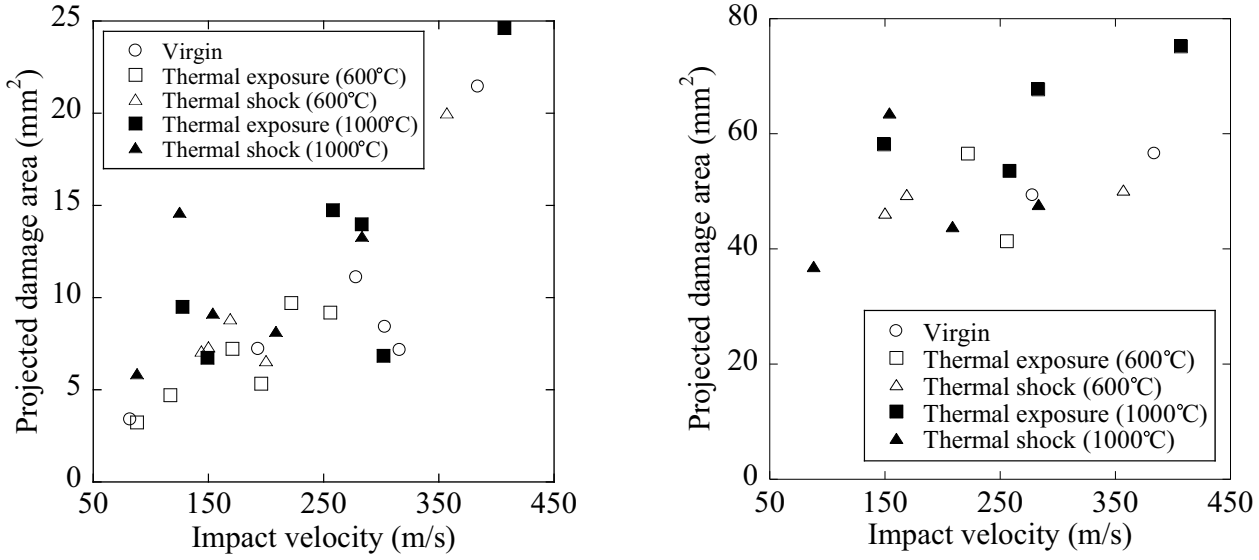

(a) Front surface (b) Back surface

Fig. 12 Relation between the projected damage area and impact velocity for all thermal-loading types.

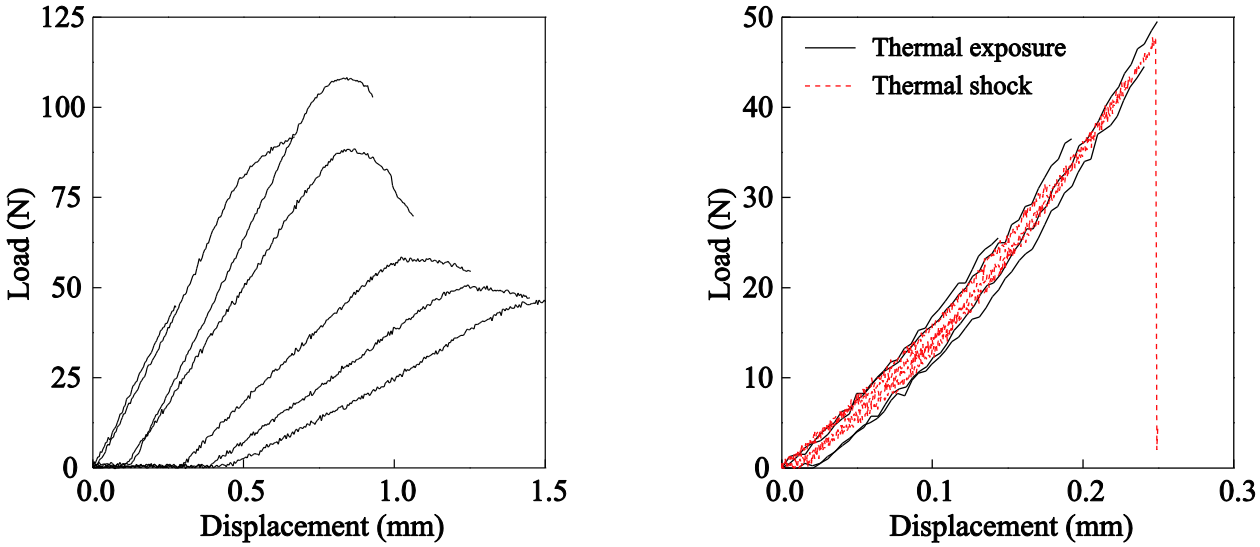

(a) Virgin (b) Thermally-loaded at 1000ºC

Fig. 13 Typical load-displacement curves from four-point flexural loading-unloading tests.

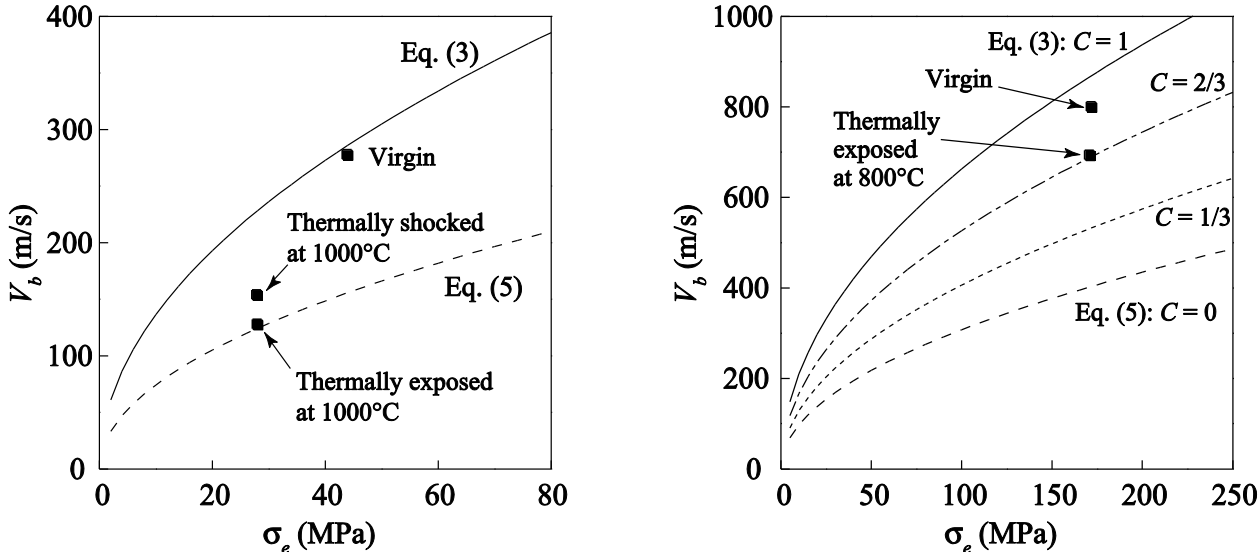

(a) Plain-woven CMC (b) 3D-woven CMC

Fig. 14 A comparison of the theoretical prediction of the ballistic limit with the experiment for virgin and thermally loaded specimens.